Biochemistry **2002,** *41,* 13309−13317

Crystal Structure of a Ternary Complex of *Tritrichomonas foetus* Inosine 5′-Monophosphate Dehydrogenase: NAD$^+$ Orients the Active Site Loop for Catalysis[†,‡]

Lu Gan,[§] Gregory A. Petsko,[||] and Lizbeth Hedstrom*[,§]

Departments of Biochemistry and Chemistry, Brandeis University, Waltham, Massachusetts 02454

Received May 24, 2002; Revised Manuscript Received August 5, 2002

ABSTRACT: Inosine 5′-monophosphate dehydrogenase (IMPDH) catalyzes the conversion of IMP to XMP with the reduction of NAD$^+$, which is the rate-limiting step in the biosynthesis of guanine nucleotides. IMPDH is a promising target for chemotherapy. Microbial IMPDHs differ from mammalian enzymes in their lower affinity for inhibitors such as mycophenolic acid (MPA) and thiazole-4-carboxamide adenine dinucleotide (TAD). Part of this resistance is determined by the coupling between nicotinamide and adenosine subsites in the NAD$^+$ binding site that is postulated to involve an active site flap. To understand the structural basis of the drug selectivity, we solved the X-ray crystal structure of the catalytic core domain of *Tritrichomonas foetus* IMPDH in complex with IMP and β-methylene-TAD at 2.2 Å resolution. Unlike previous structures of this enzyme, the active site loop is ordered in this complex, and the catalytic Cys319 is 3.6 Å from IMP, in the same plane as the hypoxanthine ring. The active site loop forms hydrogen bonds to the carboxamide of β-Me-TAD which suggests that NAD$^+$ promotes the nucleophillic attack of Cys319 on IMP. The interactions of the adenosine end of TAD are very different from those in the human enzyme, suggesting the NAD$^+$ site may be an exploitable target for the design of antimicrobial drugs. In addition, a new K$^+$ site is observed at the subunit interface. This site is adjacent to β-Me-TAD, consistent with the link between the K$^+$ activation and NAD$^+$. However, contrary to the coupling model, the flap does not cover the adenosine subsite and remains largely disordered.

Inosine monophosphate dehydrogenase (IMPDH)[1] catalyzes the rate-limiting step in the biosynthesis of guanine nucleotides: the oxidation of IMP to XMP with concomitant reduction of NAD$^+$ to NADH. IMPDH activity is essential for cell proliferation. The inhibition of IMPDH reduces guanine nucleotide levels in vivo, which impedes cellular functions such as DNA replication, RNA synthesis, and signal transduction (*2*, *3*). Several drugs target IMPDH, including the antitumor agent tiazofurin and the immunosuppressive agent mycophenolate mofetil (*4*−*6*). The active metabolite of tiazofurin is the adenine dinucleotide TAD while mycophenolate mofetil is a prodrug of mycophenolic acid (MPA) (Figure 1). These inhibitors display different affinities for enzymes from mammalian and microbial sources. MPA is a potent inhibitor of mammalian enzymes ($K_i \sim 20$ nM) but a poor inhibitor of microbial enzymes ($K_i \sim 9$ μM for *Tritrichomonas foetus* IMPDH) (*7*). β-Me-TAD is also a potent inhibitor of the human enzyme ($K_i = 0.06$ μM) but a poor inhibitor of the microbial enzymes ($K_i = 2.3$ μM) (*8*). Understanding the basis of this selectivity will

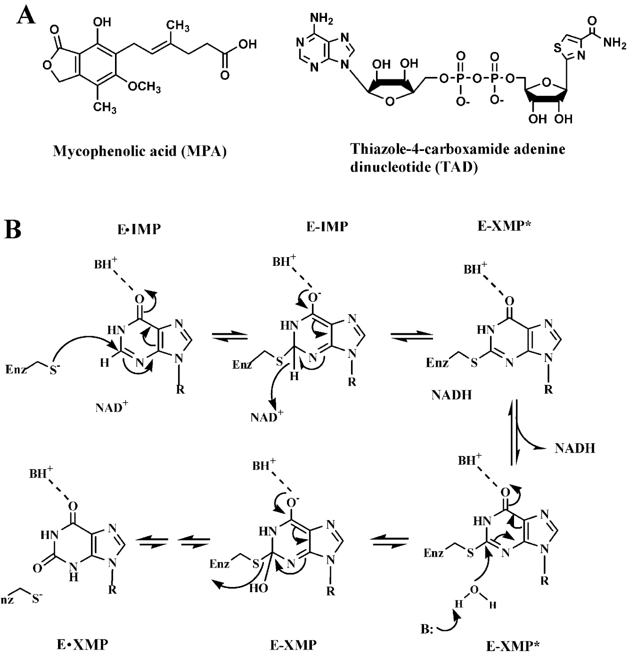

FIGURE 1: (A) IMPDH inhibitors. (B) Chemical mechanism of IMPDH reaction.

[†] Supported by NIH Grant GM54403 (L.H.) and by a grant from the Markey Charitable Trust to Brandeis University.

[‡] The crystal structure described in this paper has been deposited in the Protein DataBank as 1LRT.

[*] To whom correspondence should be addressed at the Department of Biochemistry, Brandeis University, MS 009, 415 South St., Waltham, MA 02454. E-mail: hedstrom@brandeis.edu; Phone: (781) 736-2333; Fax: (781) 736-2349.

[§] Department of Biochemistry.

[||] Department of Chemistry.

[1] Abbreviations: IMPDH, inosine 5′-monophosphate dehydrogenase; IMP, inosine 5′-monophosphate; NAD$^+$, nicotinamide adenine dinucleotide; NADH, reduced nicotinamide adenine dinucleotide; XMP, xanthosine 5′-monophosphate; ADP, adenosine 5′-diphosphate; MPA, mycophenolic acid; TAD, thiazole-4-carboxamide adenine dinucleotide; β-Me-TAD, β-methylene thiazole-4-carboxamide adenine dinucleotide; tiazofurin, 2-β-D-ribofuranosylthiazole-4-carboxamide; DTT, dithiothreitol; SAD, selenazole-4-carboxamide adenine dinucleotide.

10.1021/bi0203785 CCC: $22.00

facilitate the design of specific inhibitors for the microbial enzymes that may be developed into antimicrobial chemotherapy.

The IMPDH reaction involves two chemical transformations (Figure 1) (*7*). The active site Cys (Cys319 in *T. foetus* IMPDH) attacks the 2 position of IMP, and hydride is expelled to NAD$^+$, forming the intermediate E−XMP*. In the second transformation, water attacks the 2 position of E−XMP*, Cys is expelled, and XMP is formed. NADH release must precede the hydrolysis reaction. Most IMPDHs require K$^+$ for activity, although the *T. foetus* IMPDH appears to be independent of monovalent cations (*1*).[2] Monovalent cation activation is strongly linked to NAD$^+$ (*9*, *10*). One monovalent cation site has been identified; this site involves interactions with the carbonyl oxygen of the active site Cys and its neighboring residues (*11*). However, this site cannot explain all of the characteristics of monovalent cation activation, and some evidence exists for additional monovalent cation sites (*10*, *12*).

MPA inhibits IMPDH by specifically associating with E−XMP*, binding in the nicotinamide subsite of the dinucleotide site, and preventing hydrolysis (*11*, *13*). Two residues in the MPA site are different between *T. foetus* and human II IMPDHs: Lys310 in *T. foetus* IMPDH is Arg in the human enzyme, and Glu431 is Gln. The substitution of these residues in *T. foetus* IMPDH with their human counterparts results in a variant that is 20-fold more sensitive to MPA, but 20-fold less sensitive than human IMPDH (*14*). The remaining MPA selectivity must be determined by residues outside the MPA binding site. MPA selectivity appears to originate in the adenosine subsite of the dinucleotide site (*8*). The adenosine subsite is not conserved among IMPDHs. Multiple inhibitor experiments show that the nicotinamide and adenosine subsites are tightly coupled in *T. foetus* IMPDH but independent in the human enzyme (*8*). This coupling can account for the difference in MPA inhibition between the K310R/E431Q variant and human IMPDH. These observations suggest that MPA induces a conformational change that propagates from the nicotinamide site into the adenosine site (Figure 2).

The structure of IMPDH is characterized by disorder that suggests a dynamic active site. The enzyme is a homotetramer; each monomer contains a catalytic core domain with an α/β barrel fold and a flanking $\sim$100 residue subdomain of unknown function. The subdomain can be removed without impairing the catalytic domain (*15*). The loop that contains the active site Cys (residues 314−324) is disordered in the apoenzyme and E·XMP complexes of *T. foetus* IMPDH (*16*), but is visible in other complexes of IMPDHs from Chinese hamster (*11*), *Streptococcus pyogenes* (*17*), human (*18*), and *Borrelia burgdorferi* (*19*). This loop appears to move like a door on a hinge, but can also assume other conformations. A larger loop, termed the flap (residues 407−433), extends between β8 and α8 and is also mobile, displaying varying degrees of disorder in different complexes (*20*). This flap is believed to close over the active site in the ternary E·IMP·NAD$^+$ complex, and may be the key to understanding the coupling between the nicotinamide and adenosine sites. The distal end of the flap is disordered in the hamster E−XMP*·MPA complex (*11*); this disorder can be explained by the empty adenosine subsite. The flap is also disordered in a ternary complex containing the NAD$^+$ analogue SAD (*18*). However, in this complex the active site Cys is modified by 6-Cl-IMP, which moves the active site loop into the space usually occupied by the proximal portion of the flap. The displaced flap is disordered; however, density is observed near the adenosine of SAD that might be attributed to the distal flap. These observations suggest that the flap will close over the active site and become ordered in the E·IMP·NAD$^+$ complex, as is observed in many other enzymes.

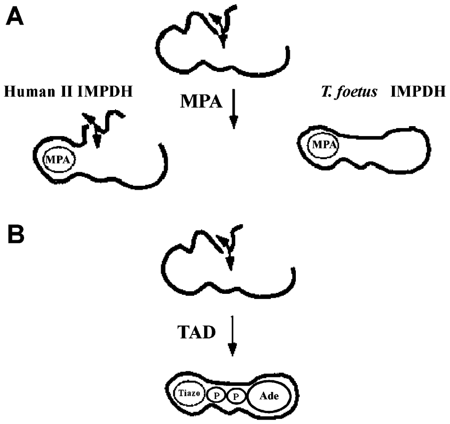

FIGURE 2: Coupling model for MPA selectivity. (A) Binding of MPA at the nicotinamide subsite of NAD$^+$ site orders the adenosine subsite in *T. foetus* IMPDH, causing lower affinity for MPA. The adenosine site is not ordered upon MPA binding in human type II IMPDH, which causes higher affinity for MPA. (B) Binding of TAD is expected to stabilize the flap and induce the formation of a closed adenosine subsite in *T. foetus* IMPDH.

We have solved the structure of a ternary complex of *T. foetus* IMPDH containing IMP and the NAD$^+$ analogue β-methylene-TAD to 2.2 Å resolution. Surprisingly, this structure reveals that the distal portion of the flap remains disordered in the ternary complex. This observation suggests that the flap may not simply form a lid over the active site. This structure suggests that NAD$^+$ orients the active site Cys for attack of IMP. In addition, the NAD$^+$ binding site of the parasite enzyme is very different from human IMPDH. Last, we observe a new K$^+$ site at the subunit interface and show that *T. foetus* IMPDH is activated by monovalent cations.

MATERIALS AND METHODS

Materials. IMP was purchased from Sigma (St. Louis). NAD$^+$ was purchased from Boehringer Mannheim. Oligonucleotides were obtained from Operon Technology. Recombinant wild-type *T. foetus* IMPDH was expressed using plasmid pTf1 and purified as previously described (*21*). β-Methylene-TAD was the generous gift of Dr. Victor Marquez (NCI).

Mutagenesis. We constructed a variant of *T. foetus* IMPDH containing only the core α/β barrel domain by deleting the subdomain residues 101−226. The plasmid containing the cDNA of the core domain was constructed by using a four-primer and three-step-PCR method with pTf1 as the template. In the first PCR, the sequence coding for residues from 1 to 100 was amplified by using 5′ primer 1 (ACC-AGC-CAA-

---

[2] Although L.H. is an author on (*1*), this paper did not originate in L.H.'s laboratory and L. H. was not involved in the experiments in question.

GAA-TTC-ATG-GCA-AAA-TAC-TAC-AAC-GAA-CCA-TGC-CAC) and 3′ primer 2 (**ATA-GCG-TTT-TTG-CGA-ATC-TTT-GAA-ATT**-TTT-GAC-AGC-ATG-GAC) with *Pfu* DNA polymerase (Stratagene, La Jolla, CA). In the second PCR, the sequence coding for residues from 227 to 503 was amplified by using 5′ primer 3 (**AAT-TTC-AAA-GAT-TCG-CAA-AAA-CGC-TAT**-TTG-GTC-GGA) and 3′ primer 4 (ACC-AGC-CAA-AAG-CTT-TTA-TTT-TGG-GTG-ATA-GTC-GTT-AAT-CCT-GTC). A portion of the sequences in primers 2 and 3 was complementary (boldface sequence) and coded for residues 98−100 and 227−232. In the third PCR, the two PCR products were annealed and elongated to generate the entire DNA sequence coding for the core domain including amino acids 1−100 and 227−503 without an exogenous linker region in between. The cDNA of core domain was then amplified by using primers 1 and 4. The PCR product was digested with *Eco*RI and *Hin*dIII (these sites are contained in primers 1 and 4, respectively), and was subcloned into the vector pKK233-3 (Pharmacia) for expression. The coding sequence of the core domain was completely sequenced using a PRISM Dyedeoxy Terminator Cycle Sequencing Kit (Applied Biosystems, Inc.) and an Applied Biosystems 373A DNA sequencer at the Brandeis Sequencing Facility. No undesired mutations were found.

Expression and Purification of the Core Domain of T. foetus IMPDH. The core domain was expressed in *E. coli* strain H712. The mutant enzyme was purified by using Cibacron Blue affinity resin and a POROS CM weak cation exchange column as previously described (*21*). The enzyme was >99% pure as judged by SDS−PAGE. IMPDH concentration was measured by using the calculated extinction coefficient $\epsilon = 40\,089\ \mathrm{M^{-1}{\cdot}cm^{-1}}$ (*22*).

Enzyme Kinetics. SDS−PAGE indicated the purified core domain had the molecular mass of 41 kDa as expected. The standard IMPDH assays contained 50 mM Tris (pH 8.0), 100 mM KCl, 3 mM EDTA, and 1 mM DTT. The production of NADH was either monitored spectrophotometrically at 340 nm at 25 °C using a Hitachi U-2000 spectrophotometer or measured by the change of fluorescence (excitation wavelength 340 nm, emission wavelength 460 nm) with a Cytofluor II multi-well plate reader (PerSeptive Biosystems, Framingham, MA). The concentrations of IMP and NAD^+ were both varied for the determination of K_m for IMP and NAD^+. For the determination of K_m and k_{cat} in the absence of K^+, standard assays contained 50 mM Tris (pH 8.0), 100 mM $N(CH_3)_4{}^+Cl^-$, and 1 mM DTT. $N(CH_3)_4{}^+Cl^-$ was used in the assay to maintain the ion strength in the absence of K^+. $N(CH_3)_4{}^+Cl^-$ neither activates nor inhibits IMPDH. The concentration of IMP or NAD^+ was varied at saturated concentration of the other substrate. Initial velocity data were fit to the Michaelis−Menten equation and an uncompetitive substrate inhibition equation by using software SigmaPlot 2000 (SPSS, Inc.):

$$v = V_m[\mathrm{IMP}]/(K_a + [\mathrm{IMP}])$$

$$v = V_m[\mathrm{NAD^+}]/(K_b + [\mathrm{NAD^+}] + [\mathrm{NAD^+}]^2/K_{ii})$$

where v is the initial velocity, V_m is the maximal velocity, K_a and K_b are the Michaelis constants for IMP and NAD^+, respectively, and K_{ii} is the substrate inhibition constant for NAD^+.

Potassium Activation. Activation of *T. foetus* IMPDH by K^+ exhibited saturated kinetics. Reactions were performed in 0.4 mM IMP, 1 mM NAD^+, 50 mM Tris (pH 8.0), various concentration of KCl, and 1 mM DTT at 25 °C. Appropriate concentrations of $N(CH_3)_4{}^+Cl^-$ were added to the assay to maintain constant ionic strength. Data were fit to the Michaelis−Menten equation:

$$v/[\mathrm{E}] = V_m[\mathrm{M}]/(K_m + [\mathrm{M}]) + v_0/[\mathrm{E}]$$

where v is the initial velocity, [E] is the enzyme concentration, V_m is the maximal rate, [M] is the concentration of K^+, K_m is the concentration of K^+ at half the maximal velocity, and v_0 is the basal velocity in the absence of K^+.

Crystallization, Data Collection, and Processing. Crystals of the core domain of *T. foetus* IMPDH were grown at room temperature with the sitting-drop vapor-diffusion method. The initial crystallization conditions were evaluated using the Crystal Screen I and II Kits (Hampton Research, Laguna Niguel, CA). The crystals for this study were obtained by mixing the protein solution [containing 2 mg/mL mutant IMPDH, 50 mM Tris-HCl (pH 7.5), 5% glycerol, 40 mM IMP, 3.5 mM β-methylene-TAD, 1 mM DTT] with reservoir solution [containing 10% PEG 10 000, 100 mM MES (pH 6.25), 120 mM KCl, 20% glycerol, 2% β-octylglucoside (w/v), 1 mM DTT] at a 1:1 ratio. Thin and planklike crystals can be observed in 24 h. The crystals grew to a maximal size of 0.6 mm × 0.2 mm × 0.08 mm. A crystal was soaked in the cryo-protectant reagent Paratone-N (Hampton Research, Laguna Niguel, CA) for a few seconds. The crystal was loop-mounted and flash-frozen in liquid nitrogen stream. Data were collected from a single crystal at 100 K on the CCD detector on beamline 14BMC at Advanced Photon Source (Argonne National Laboratory, Argonne, IL). The X-ray wavelength was 1.00 Å. The distance between the crystal and detector was 180.0 mm. Totally, 160 frames were collected with 1° oscillation and 15 s exposure per frame. The data were processed and scaled with DENZO and SCALEPACK (*23*). Data collection statistics are outlined in Table 1. The asymmetric unit contained a dimer. The quaternary structure of the enzyme is a tetramer, consistent with the oligomeric state of the native enzyme.

Molecular Replacement and Refinement. The molecular replacement method was employed to solve the structure. In the 2.6 Å resolution structure of *T. foetus* IMPDH [PDB entry 1AK5; (*16*)], the subdomain (residues 102−221), active site flap (residues 413−431), and C-terminus (residues 484−503) are disordered. The active site loop (residues 314−324) is modeled as a poly-Ala chain. In this study, the tetramer structure of wild-type *T. foetus* IMPDH was truncated to a dimer to build up the search model. The poly-Ala chain substituted for the active site loop in the original structure was omitted from the search model. The program package AMORE (*24*) was used to solve the phase problem. The cross-rotation function was performed to find out the orientation of the search model in the lattice with data from 20.0 to 4.0 Å. Four solutions with equal peak values (correlation coefficients of 16.0) were generated by cross-rotation search, and were related symmetrically by a rotation of 90°. This indicated the existence of a 4-fold noncrystallographic axis within the structure. Subsequent translation search generated the positions of two dimers in the unit cell.

Table 1: Statistics for Data Collection and Refinement

Data Collection	
temperature	100 K
space group	$P2_12_12_1$
unit cell (Å)	
a	96.14
b	112.37
c	161.99
$\alpha = \beta = \gamma$ (deg)	90.00
resolution (Å)	2.2
total no. of reflections	356029
no. of unique reflections	87015 [$I/\sigma(I) > 0$]
overall $\langle I/\sigma(I) \rangle$	>12
completeness of data (%; overall/2.20−2.28 Å)	96.8/91.3
R-merge[a] (%; overall/2.20−2.28 Å)	8.9/39.8
Refinement	
resolution range (Å)	8.0−2.2
reflections used (working/free)	71997/8033
temperature factor model	restrained group
R-factor[b]/*R*-free (%)	21.8/24.6
model used in refinement	(tetramer)
total non-hydrogen atoms in protein	10295
no. of waters	543
no. of IMP	4
no. of β-methylene-TAD	4
no. of potassium ion	4
no. of β-octylglucoside	2
no. of Tris	12
rms deviations from ideal geometry[c]	
bond length (Å)	0.006
bond angles (deg)	1.27
dihedral angles (deg)	22.9
improper angles (deg)	1.03

[a] *R*-merge = $\Sigma|I_{obs} - I_{avg}|/\Sigma I_{avg}$, over all symmetry-related observations. [b] *R*-factor = $\Sigma|F_{obs} - F_{avg}|/\Sigma F_{avg}$, over all reflections. [c] Engh and Huber parameters were used in refinement.

Further refinement of these two dimers together resulted in the final solutions with equal correlation coefficients of 57.9 and *R*-factors of 39.7%. The initial structures of the two dimers were obtained by applying the final solutions to produce the coordinate files. The two dimers form a tetramer. The program packages CNS 1.0 (*25*) and O 7.0 (*26*) were used in the subsequent structural refinement and model building. After rigid body and simulated annealing refinement with NCS restraints, the $2F_o-F_c$ density map and $1F_o-F_c$ difference map were generated. Clear and continuous electron density was observed in the area of the active site loop. The difference map also showed clear electron density in the active site region corresponding to the bound substrate IMP and β-methylene-TAD. The models for IMP and β-methylene-TAD were fit to this density. Water molecules were added into the model at the late stage of the refinement. The electron density for one water molecule in proximity to the NAD^+ binding site was slightly larger than that for other water molecules. This molecule was finally modeled as a potassium ion. It was coordinated to main chain carbonyl groups of Gly20, Asn460, and Phe266′, the side chain carboxylate of Asp264′, and the hydroxyl of Ser22 (The symbol ′ denotes the residue contributed by the adjacent monomer). In the subsequent cycles of refinement, the residues of the active site loop and flap region missing in the original structure were added to the new model gradually. Conjugate-gradient minimization and individual *B*-factor refinement were performed after new models were built to fit the density in each refinement cycle. The final *R*-factor and *R*-free are 21.8% and 24.6%, respectively, for the reflections with resolution between 8.0 and 2.2 Å. The final tetramer model contains 340 of 377 residues in monomer D, 338 in monomer A, and 334 in monomers B and C. There are also 543 water molecules, 12 molecules of Tris, and 2 molecules of β-octylglucoside in the whole tetramer structure. The β-octylglucoside molecules are bound at the adenosine end of the binding site for β-methylene-TAD. Each monomer contains one molecule of IMP, one molecule of β-methylene-TAD, and one molecule of potassium ion. Residues 100−227−228−229−230 in the linker region of the core domain, 417−430 in the active site flap, and 486−503 in the C-terminus are missing in the final structure. Residues 320−322 are also missing in monomers A, B, and C. Analysis of the model with PROCHECK (*34*) showed that 90.6% of the residues are in the most favorable regions and 8.8% of the residues are in additionally allowed regions. The data collection and refinement statistics are reported in Table 1.

Table 2: Michaelis−Menten Parameters for *T. foetus* Wild-Type IMPDH and Core Domain

	[KCl] = 100 mM[a]		[KCl] = 0 mM[b]	
	wild type[c]	core domain	wild type	core domain
k_{cat} (s^{-1})	1.9 ± 0.2	1.4 ± 0.1	0.016 ± 0.001	0.010 ± 0.001
K_m(IMP) (μM)	1.7 ± 0.4	3.0 ± 0.6	2.6 ± 0.7	2.4 ± 0.6
$K_m(NAD^+)$ (μM)	150 ± 30	110 ± 10	1100 ± 200	1200 ± 300
$K_{ii}(NAD^+)$ (μM)	6800 ± 1800	2900 ± 200	na[d]	na[d]

[a] Reactions were performed in 50 mM Tris (pH 8.0), 100 mM KCl, 3 mM EDTA, and 1 mM DTT at 25 °C. [b] Reactions were performed in 50 mM Tris (pH 8.0), 100 mM $N(CH_3)_4{}^+Cl^-$, and 1 mM DTT at 25 °C. [c] These values are from ref (*21*). [d] Not applicable.

RESULTS

Characterization of the Core Domain. Nimmesgern and colleagues have shown that deletion of the subdomain has no effect on enzymatic activity (*15*). To facilitate crystallization, we deleted the subdomain (residues 101−226) from *T. foetus* IMPDH by linking residue 100 directly to residue 227. The kinetic parameters of this core domain are similar to those of wild-type enzyme (Table 2). The K_m values of NAD^+ and IMP are indistinguishable from those of wild-type, while the value of k_{cat} is reduced by 30%. The core domain is slightly more prone to NAD^+ substrate inhibition, with the value of K_{ii} reduced 2.3-fold. These observations demonstrate that the deletion of the subdomain does not significantly perturb IMPDH function.

General Features of the Core Domain Structure. The crystal structure of the core domain in complex with IMP and an NAD^+ analogue, β-Me-TAD, was solved to 2.2 Å resolution by molecular replacement as described under Materials and Methods. In β-Me-TAD, the bridging O is replaced with a methylene group. The *R*-factor of the final model is 21.8% (*R*-free = 24.6%) for the data between 8.0 and 2.2 Å resolution (Table 1). In the final model, monomer D contains 340 of 377 residues, 1 molecule of IMP, 1 molecule of β-Me-TAD, and 1 potassium ion per monomer. IMP and β-Me-TAD were defined unambiguously based on the F_o-F_c omit map. Figure 3 shows the ribbon diagram of monomer D, and the bound IMP, β-Me-TAD, and potassium ion. Symmetry packing of the protein also generates a

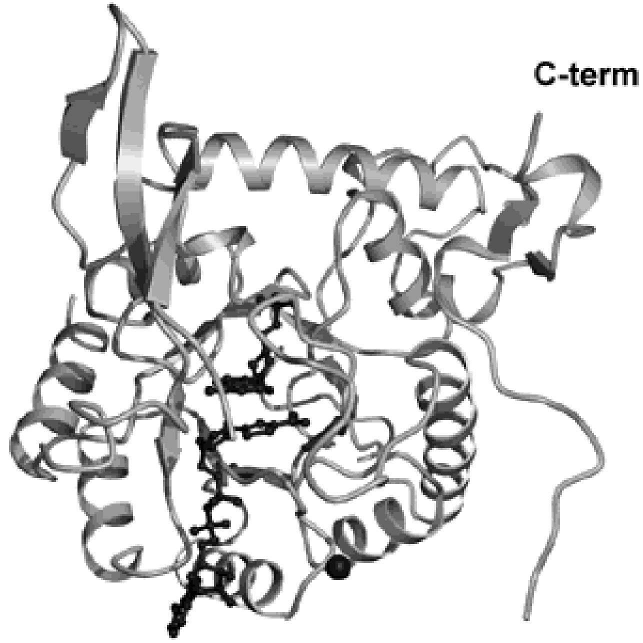

FIGURE 3: Ribbon diagram of *T. foetus* IMPDH core domain (gray). IMP and β-Me-TAD are shown at the active site as ball-and-stick models (black). A potassium ion close to the dinucleotide site is shown as a space-fill model (black). This figure was produced with Molscript v2.1 (*33*).

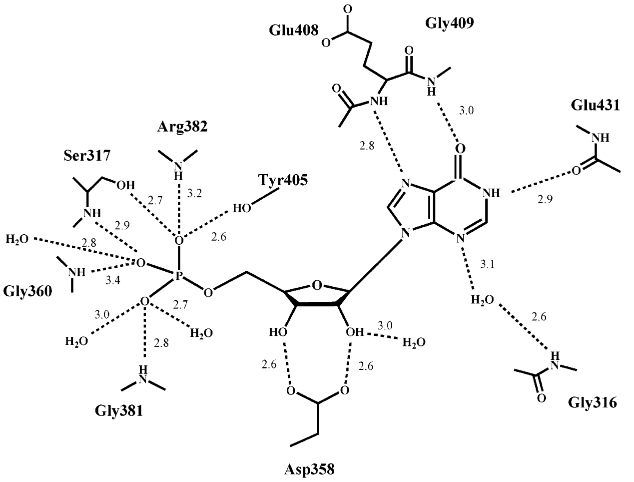

FIGURE 4: Schematic representation of the interactions between IMP and *T. foetus* IMPDH.

binding site for β-octylglucoside between two tetramers. The missing residues are from the flexible segments such as the linker region of the core domain (residues 100−227−228−229−230), the active site flap (residues 417−430), and the C-terminus (residues 486−503). Analysis of the structure with PROCHECK (*34*) shows that conformations of 90.6% residues are in most favorable regions, and 8.8% in additionally allowed regions. The core domain forms an eight-stranded parallel α/β barrel as in the full-length enzyme. The active site loop (residues 314−324, including Cys319), which is largely missing in the structures of apoenzyme and E·XMP complexes, becomes ordered in the ternary complex. However, the flap remains largely disordered despite the presence of an NAD$^+$ analogue, although four more residues are visible than in the apoenzyme and E·XMP complexes.

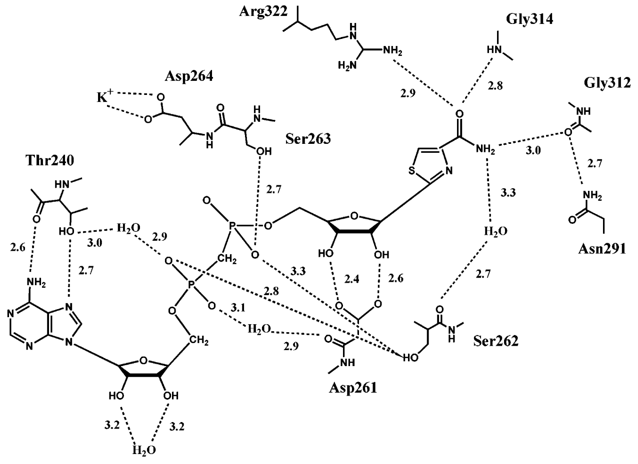

FIGURE 5: Schematic representation of the interactions between β-methylene-TAD and *T. foetus* IMPDH.

The IMP Binding Site. Figure 4 shows the interactions between the enzyme and IMP. Similar interactions are found between enzyme and XMP (*16*), with the following exceptions: (1) The active site loop is ordered and Sγ of Cys319 is 3.6 Å from C2 of IMP, in the same plane as the hypoxanthine ring. (2) We did not observe an interaction between the guanidinium group of Arg382 and the phosphate of IMP as reported in the E·XMP complex (*16*). Instead, Arg382 points away from IMP, and the phosphate interacts with the hydroxyl group of Ser317. (3) A hydrogen bond forms between N1 of the hypoxanthine ring and the main-chain carbonyl oxygen of Glu431. (4) A van der Waals interaction is observed between the side chain of Ile318 and the hypoxanthine ring.

The Dinucleotide Binding Site. The hydrogen bond interactions between β-Me-TAD and *T. foetus* IMPDH are illustrated in Figure 5. β-Me-TAD lies in the cleft between two adjacent monomers, and the thiazole ring stacks against the hypoxanthine ring of IMP, as observed in the human SAD complex (*18*). However the carboxamide and adenosine moieties of β-Me-TAD make very different interactions in the *T. foetus* structure.

(1) The interactions between the active site loop and the carboxamide of β-Me-TAD are the most striking feature of the ternary complex. The carboxamide group forms hydrogen bonds with Ser262, Gly312, Gly314, and Arg322. These interactions are not observed in the SAD complex due to the displacement of the loop by covalent modification of the enzyme (*18*). Instead the carboxamide of SAD forms hydrogen bonds with the side chain of Asn303. The homologous Asn291 points away from the carboxamide group in our structure, forming hydrogen bonds with Gly312 of the active site loop.

(2) The adenine ring inserts into the space between the side-chain rings of Phe282 and His253 in the human structure (*18*). In the *T. foetus* IMPDH complex, the adenine stacks against the indole ring of Trp269 and forms van der Waals contact with the guanidine moiety of Arg241 (Figure 6). Two molecules of β-octylglucoside flank the adenine end of β-Me-TAD in a site formed by crystal packing.

(3) Unlike human IMPDH, no interactions are observed between β-Me-TAD and the adjacent monomer. In human IMPDH, the side chain of Gln469 in the adjacent monomer forms hydrogen bonds with the ribosyl hydroxyl groups of

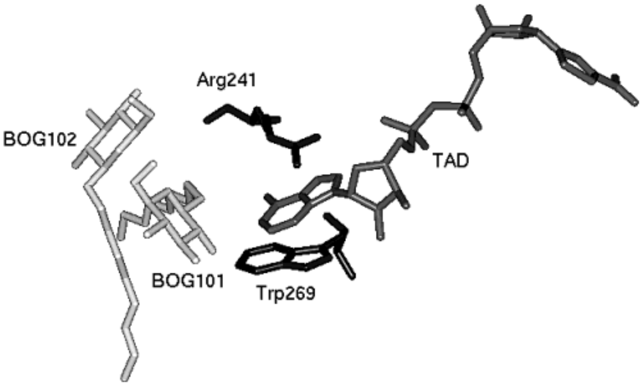

FIGURE 6: Binding site of the adenine ring of β-methylene-TAD (dark gray, TAD). The adenine ring stacks with Trp269 (black) and forms van der Waals contact with Arg241 (black). Two molecules of β-octylglucoside (light gray, BOG101 and BOG102) flank the end of this site. This figure was produced with Molscript v2.1 (*33*).

the adenosine moiety. In *T. foetus* IMPDH, the homologous residue Cys459 forms a disulfide bond with Cys26, leaving a cavity near the two hydroxyls. This disulfide bond is also observed in the other *T. foetus* IMPDH structures (*16*). We suspect that this disulfide bond is an artifact of crystallization because the enzyme is stored in the presence of dithiothreitol. Reduced Cys459 can be modeled to within 4 Å of the adenosine hydroxyls, so that an additional adjustment would be necessary to form hydrogen bonds. In human IMPDH, the side chain hydroxyl of Thr45 also hydrogen bonds to N3 of the adenine ring. However, the homologous residue in *T. foetus* is Ile27. No close contact between this residue and the adenine ring is observed.

The Active Site Flap. Contrary to expectations, the flap is only slightly more ordered in the presence of β-Me-TAD, with four more flap residues (413−416) visible in the $F_o - F_c$ difference map compared with the E·XMP complex. The last two residues, Asn415 and Trp416, are in an α-helical region. Residues 417−430 are still missing in the ternary complex, leaving one side of NAD$^+$ binding cleft exposed to solvent. Symmetry packing of the structure indicates there is still plenty of space near β-Me-TAD to accommodate the distal flap.

The Potassium Binding Site. A new potassium binding site is identified at the interface between two monomers in the E·IMP·β-Me-TAD complex, formed by three main-chain carbonyls from Gly20, Asn460, and Phe266′, the side-chain hydroxyl of Ser22, and the side-chain carboxylate of Asp264′ (Figure 7; the symbol ′ denotes a residue from the adjacent monomer). This hexagonal coordination pattern is commonly observed in K$^+$ binding sites (*27*−*29*). The average distance between K$^+$ and protein ligands is 2.6 Å. Further, Asp264 is adjacent to the residues that comprise the TAD binding site (Asp261, Ser262, and Ser263, Figure 5), which suggests that K$^+$ will facilitate NAD$^+$ binding.

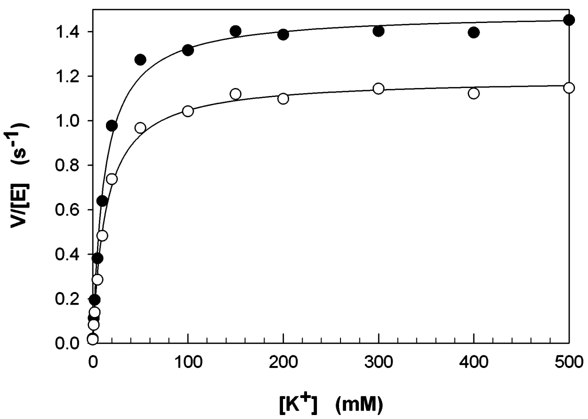

FIGURE 8: K$^+$ activation of *T. foetus* wild-type IMPDH (●) and the catalytic domain (○). Reactions were performed in 0.4 mM IMP, 1 mM NAD$^+$, 50 mM Tris (pH 8.0), various concentrations of KCl, and 1 mM DTT at 25 °C. Appropriate concentrations of $N(CH_3)_4{}^+Cl^-$ were added to the assay to maintain the total concentration of monovalent ion [$N(CH_3)_4{}^+$ and K$^+$] at 500 mM.

Monovalent Cation Activation of T. foetus IMPDH. The observation of K$^+$ in our structure led us to reinvestigate the monovalent cation dependence of *T. foetus* IMPDH. Contrary to a previous report (*1*), *T. foetus* IMPDH is activated ∼100-fold by K$^+$ with a K_{app} of 12 mM (Figure 8). The core domain is also activated by K$^+$, with a K_{app} of 14 mM (Figure 8). The kinetic parameters of wild-type *T. foetus* IMPDH and the core domain measured in the absence of K$^+$ are summarized in Table 2. In the absence of K$^+$, the values of k_{cat} decrease by ∼100 fold and the values of K_m for NAD$^+$ increase by ∼8-fold while the K_m values of IMP are relatively unchanged. NAD$^+$ inhibition is not observed in the absence of K$^+$. These results demonstrate that K$^+$ activation is linked to NAD$^+$ as observed in other IMPDHs (*9*, *10*, *12*, *30*). We were careful to hold ionic strength and pH constant and to eliminate sources of contaminating

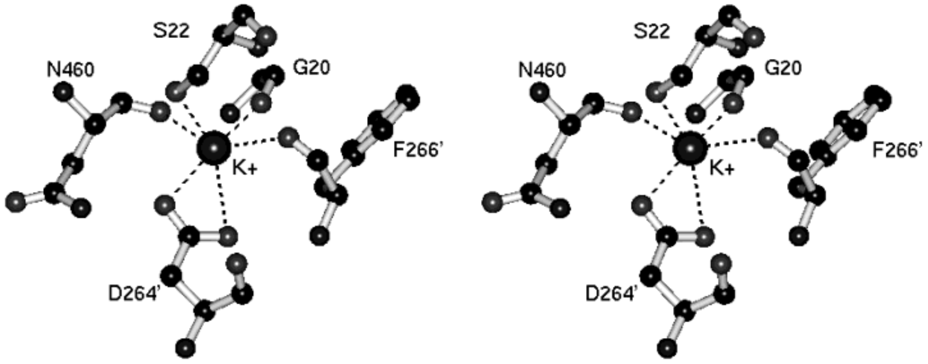

FIGURE 7: Stereoview of a ball-and-stick model of the K$^+$ binding site 2. The dashed lines indicate the coordination of protein ligands to K$^+$ ion. The K$^+$ to protein ligand distances are as follows: Gly20 carbonyl, 2.5 Å; Ser22 hydroxyl, 2.6 Å; Asn460 carbonyl, 2.8 Å; Asp264′ carboxylate, 2.4 and 2.8 Å; Phe266′ carbonyl, 2.7 Å. (The symbol ′ denotes the residue from the adjacent monomer.) This figure was produced with Molscript v2.1 (*33*).

monovalent cations (for example, by using substrate acids instead of salts). These factors may have confounded earlier experiments.

DISCUSSION

The crystal structure E·IMP·β-Me-TAD complex of *T. foetus* IMPDH described herein provides new insights into the mechanism of the IMPDH reaction and refines the model for MPA and TAD selectivity.

The NAD$^+$ Site. The most striking feature of our structure is the interaction between the carboxamide of tiazofurin and Gly312, Gly314, and Arg322 of the active site loop (Figure 5). These interactions are likely to be general: Gly312 and Gly314 are conserved among all IMPDHs. However, while prokaryotic IMPDHs generally contain Arg322, most eukaryotic organisms contain Gln at this position. The evolutionary significance of this difference is not clear, but it seems likely that Gln could also form hydrogen bonds with NAD$^+$. The interactions between the loop and β-Me-TAD suggest that NAD$^+$ orients the active site loop and Cys319 for attack of IMP.

As first noted by Goldstein, the adenosine end of the NAD$^+$ site varies widely among different IMPDHs (*17, 18*). The adenine ring stacks between the side chains of His253 and Phe282 in the human type II isozyme. These residues are replaced by Arg241 and Trp269 in *T. foetus* IMPDH, offering a strategy for the design of specific inhibitors of the *T. foetus* enzyme. For example, an anionic inhibitor might interact with Arg241 in *T. foetus* IMPDH but would be unable to bind to the human isozyme. The sequence variation in this region is even more striking for prokaryotic enzymes which lack the aromatic residues of the adenosine binding sites of human and *T. foetus* IMPDH (*31*). This variation provides an attractive target for drug design.

T. foetus IMPDH has lower affinity for β-Me-TAD than human IMPDH [2.3 μM vs 0.06 μM, respectively (*8*)]. However, we cannot attribute this difference in affinity to specific interactions at the NAD$^+$ site. First, we cannot determine the energy of the stacking interactions at the NAD$^+$ site. More importantly, affinity is also determined by the energetics of the conformational rearrangements induced when inhibitor binds. When the coupling of the nicotinamide and adenosine subsites is taken into account, the energy associated with TAD binding to *T. foetus* IMPDH is actually 1.0 kcal/mol greater than for the human enzyme (*8*).

The Reaction Coordinate. IMPDH appears to undergo several conformational transitions as the reaction proceeds. Although utilizing IMPDHs from different sources, the structures of the apoenzyme, E·IMP, E·IMP·β-Me-TAD, and E−XMP*·MPA complexes appear to capture the enzyme at different stages of the catalytic transformation. The active site loop and flap are largely disordered in the absence of substrates. The Cα atoms of the IMP site (defined in Figure 4) can be aligned with a RMSD of only 0.3−0.4 Å (Table 3), which suggests that these residues remain stationary during the reaction. In contrast, the conformation of the active site loop varies from disordered to the defined positions of Figure 9. In the E·IMP complex, the active site Cys is poised above the hypoxanthine ring, in position for nucleophillic attack. In the β-Me-TAD complex, both IMP and the loop adjust so that Cys is now in the plane of the hypoxanthine ring (Figure 9A). This movement is necessary to form the hydrogen bonds between the carboxamide of TAD and the loop and the stacking interactions between the thiazole and hypoxanthine rings. The conformation of IMP is now similar to that of E−XMP* (Figure 9B). Presumably, NAD$^+$ also triggers this movement, promoting the formation of E−XMP* by positioning the active site loop. Although we expect that a tetrahedral adduct forms between IMP and Cys319 (Figure 1), we do not observe this adduct in the E·IMP·β-Me-TAD complex. This is not surprising because the equilibrium for formation of this adduct is very unfavorable.

Table 3: Comparison of the Positions of IMP Site Residues from *T. foetus* E·IMP·β-Me-TAD, *S. pyogenes* E·IMP, and Chinese Hamster E−XMP*·MPA Structures

rmsd by least-squares analysis (Å)	IMP site residues[a,b]	loop only[a,c]
E·IMP·β-Me-TAD vs E·IMP	0.4	1.3
E·IMP·β-Me-TAD vs E−XMP*·MPA	0.3	1.2
E·IMP vs E−XMP*·MPA	0.3	0.4

[a] Homologous Cα atoms are compared. [b] The eight IMP site residues in least-squares analysis are D358, G360, G381, R382, Y405, E408, G409, and E431 in *T. foetus* IMPDH as shown in Figure 4. R382 is replaced by Ser in *S. pyogenes* and in Chinese hamster IMPDHs. E431 is replaced by Gln in hamster IMPDH. Other residues are the same as *T. foetus* enzyme. [c] Active site loop contains residues 309−323 in *T. foetus* IMPDH, 300−314 in *S. pyogenes* IMPDH, and 321−335 in hamster IMPDH.

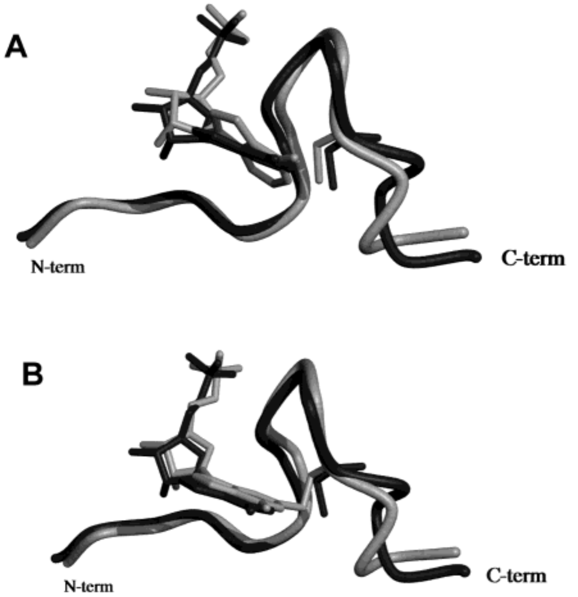

FIGURE 9: Comparison of active site loop and IMP conformations in (A) *T. foetus* E·IMP·β-Me-TAD complex (black) and *S. pyogenes* E·IMP complex (gray) and (B) *T. foetus* E·IMP·β-Me-TAD complex (black) and Chinese hamster E−XMP*·MPA complex (gray). IMP and catalytic Cys are shown in stick representation. This figure was produced with Molscript v2.1 (*33*).

The stability of the active site structure appears to vary among different IMPDHs, which may account for different kinetic properties of the various enzymes. For example, the large values of k_{cat} generally observed in bacterial enzymes might be attributed to the greater stability of the active site loop structures. This stability is illustrated in the apoenzyme structure of *Borrelia burgdorferi* IMPDH and the E·IMP complex of *S. pyogenes*, where the active site loop can be clearly observed. In contrast, the active site loop is disordered in the comparable structures of the *T. foetus* enzyme. The C-terminal segment adjacent to the active site loop remains disordered even in the E•IMP•β-Me-TAD complex, further suggesting that the structure is less stable than in the bacterial enzymes.

The flap also moves as the reaction proceeds. The proximal region of the flap closes over IMP and NAD$^+$, shielding the site of chemical transformation from water. However, the distal region of the flap remains disordered. The stability of the flap structure is also likely to be an important determinant of catalytic efficiency.

The Mechanism of K$^+$ Activation. We have shown that *T. foetus* IMPDH is activated by monovalent cations, as observed with all other IMPDHs. The specificity of monovalent cation activation varies greatly among different IMPDHs, and the structural basis of this activation is not understood (*30*). As seen in Table 2, K$^+$ activation is linked to the K_m of NAD$^+$ and k_{cat}, as observed with other IMPDHs (*9, 10*). Although one K$^+$ site has been identified (site 1; discussed more below), it cannot account for all of the features of K$^+$ activation (*10, 12*). In addition, some kinetic evidence suggests that two K$^+$ sites may be present (*10*).

We have discovered a new K$^+$ site that is clearly linked to NAD$^+$ binding. This site is formed by three main-chain carbonyls from Gly20, Asn460, and Phe266′, the side-chain hydroxyl of Ser22, and the side-chain carboxylate of Asp264′ (where ′ denotes the adjacent monomer) (Figure 7). These residues are not conserved among IMPDHs. This second K$^+$ site is adjacent to the NAD$^+$ site; residues Asp261, Ser262, and Ser263 interact with β-Me-TAD while Asp264 is a component of the K$^+$ binding site (Figure 7). This K$^+$ site may also exist in other complexes of the *T. foetus* enzyme (*16*). Modeling a K$^+$ into the equivalent site in apoenzyme indicates the distance between K$^+$ and protein ligands 0.3 Å longer than in the ternary complex, suggesting that K$^+$ affinity decreases in the absence of NAD$^+$.

Although K$^+$ site 1 has only been reported in the hamster E−XMP*•MPA complex, we believe that it is likely to be present in all IMPDHs. This K$^+$ ion is coordinated to the main chain carbonyls of the active site loop and the C-terminus of an adjacent subunit, residues Gly326, Gly328, Cys331, Glu500′, Gly501′, and Gly502′ (*32*). The active site loop residues and Glu500′ are conserved among all IMPDHs, so it seems likely that this site is also found in all IMPDHs. This site also appears to be present in the *S. pyogenes* E•IMP complex (*17*). Inspection of this structure reveals that a water molecule is modeled within 2.4−2.7 Å of the active site loop carbonyls that form the K$^+$ site. It seems likely that this water molecule is actually an NH_4^+ from the crystallization solution. The K$^+$ site 1 could easily be envisioned to facilitate both NAD$^+$ binding and k_{cat} via the active site loop. However, while K$^+$ site 1 is probably found in all IMPDHs, it does not exist in all complexes. The *T. foetus* apoenzyme, E•XMP, and E•IMP•β-Me-TAD structures all contain disorder in the ligands that comprise the K$^+$ site, indicating that the K$^+$ site 1 is not present. We believe that the K$^+$ site 1 becomes available as the reaction proceeds, perhaps acting to stabilize the E−XMP* intermediate.

Model for MPA Selectivity. A conformational change propagates from the nicotinamide half of the NAD$^+$ site into the adenosine subsite which determines the drug selectivity (*8*). According to the coupling model proposed previously, binding of MPA or other NAD$^+$ analogues in the nicotinamide subsite will stabilize the active site flap and induce a closed adenosine subsite (*8*). However, this is not observed in the E•IMP•β-Me-TAD ternary structure. The distal flap is still disordered, similar to the distal flap in the E−XMP*•MPA complex. This suggests that the flap does not close over the adenosine site as generally supposed. A different conformational change must account for the coupling between the nicotinamide and adenosine subsites. We have recently discovered a new conformation where the flap moves into the NAD$^+$ site (L.G., unpublished experiments). This new closed conformation can account for the coupling across the NAD$^+$ site.

ACKNOWLEDGMENT

We thank Dr. Karen Allen (School of Medicine, Boston University) for assistance in X-ray crystallographic data collection and Dr. Victor Marquez (NCI) for providing β-methylene-TAD and acknowledge the work of Jennifer Digits in initially characterizing K$^+$ activation of *T. foetus* IMPDH.

REFERENCES

1. Verham, R., Meek, T. D., Hedstrom, L., and Wang, C. C. (1987) *Mol. Biochem. Parasitol. 24*, 1−12.
2. Weber, G. (1983) *Cancer Res. 43*, 3466−3492.
3. Weber, G., Prajda, N., Abonyi, M., Look, K. Y., and Tricot, G. (1996) *Anticancer Res. 16*, 3313−3322.
4. Boritzki, T. J., Berry, D. A., Besserer, J. A., Cook, P. D., Fry, D. W., Leopold, W. R., and Jackson, R. C. (1985) *Biochem. Pharmacol. 34*, 1109−1114.
5. Allison, A. C., and Eugui, E. M. (2000) *Immunopharmacology 47*, 85−118.
6. Robins, R. K., Revankar, G. R., McKernan, P. A., Murray, B. K., Kirsi, J. J., and North, J. A. (1985) *Adv. Enzyme Regul. 24*, 29−43.
7. Hedstrom, L. (1999) *Curr. Med. Chem. 6*, 575−597.
8. Digits, J. A., and Hedstrom, L. (2000) *Biochemistry 39*, 1771−1777.
9. Heyde, E., Nagabhushanam, A., Vonarx, M., and Morrison, J. (1976) *Biochim. Biophys. Acta 429*, 645−660.
10. Kerr, K. M., Cahoon, M. C., Bosco, D. A., and Hedstrom, L. (2000) *Arch. Biochem. Biophys. 375*, 131−137.
11. Sintchak, M. D., Fleming, M. A., Futer, O., Raybuck, S. A., Chambers, S. P., Caron, P. R., Murcko, M., and Wilson, K. P. (1996) *Cell 85*, 921−930.
12. Markham, G. D., Bock, C. L., and Schalk-Hihi, C. (1999) *Biochemistry 38*, 4433−4440.
13. Link, J. O., and Straub, K. (1996) *J. Am. Chem. Soc. 118*, 2091−2092.
14. Digits, J. A., and Hedstrom, L. (1999) *Bichemistry 38*, 15388−15397.
15. Nimmesgern, E., Black, J., Futer, O., Fulghum, J. R., Chambers, S. P., Brummel, C. L., Rayuck, S. A., and Sintchak, M. D. (1999) *Protein Expression Purif. 17*, 282−289.
16. Whitby, F. G., Luecke, H., Kuhn, P., Somoza, J. R., Huete-Perez, J. A., Philips, J. D., Hill, C. P., Fletterick, R. J., and Wang, C. C. (1997) *Biochemistry 36*, 10666−10674.
17. Zhang, R.-G., Evans, G., Rotella, F. J., Westbrook, E. M., Beno, D., Huberman, E., Joachimiak, A., and Collart, F. R. (1999) *Biochemistry 38*, 4691−4700.
18. Colby, T. D., Vanderveen, K., Strickler, M. D., Markham, G. D., and Goldstein, B. M. (1999) *Proc. Natl. Acad. Sci. U.S.A. 96*, 3531−3536.
19. McMillan, F. M., Cahoon, M., White, A., Hedstrom, L., Petsko, G. A., and Ringe, D. (2000) *Biochemistry 39*, 4533−4542.
20. Goldstein, B. M., and Colby, T. D. (1999) *Curr. Med. Chem. 6*, 519−536.
21. Digits, J. A., and Hedstrom, L. (1999) *Biochemistry 38*, 2295−2306.

22. Gill, S. C., and von Hippel, P. H. (1989) *Anal. Biochem. 182*, 319−326.
23. Otwinowski, Z. (1993) in *Data Reduction and Processing* (Sawyer, L., Isaacs, N., and Bailey, S., Eds.) SERC Daresbury Laboratory, Warrington, England.
24. Navaza, J. (1994) *Acta Crystallogr. A50*, 157−163.
25. Brunger, A. T., Adams, P. D., Clore, G. M., DeLano, W. L., Gros, P., Grosse-Kunstleve, R. W., Jiang, J. S., Kuszewski, J., Nilges, M., Pannu, N. S., Read, R. J., Rice, L. M., T., S., and Warren, G. L. (1998) *Acta Crystallogr., Sect. D: Biol. Crystallogr. 54*, 905−921.
26. Jones, T. A., Zou, J.-Y., Cowan, S. W., and Kjeldgaard, M. (1991) *Acta Crystallogr. A 47*, 110−119.
27. Larsen, T. M., Laughlin, L. T., Holden, H. M., Rayment, I., and Reed, G. H. (1994) *Biochemistry 33*, 6301−6309.
28. Thoden, J. B., Raushel, F. M., Benning, M. M., Rayment, I., and Holden, H. M. (1999) *Acta Crystallogr. D55*, 8−24.
29. Shibata, N., Masuda, J., Tobimatsu, T., Toraya, T., Suto, K., Morimoto, Y., and Yasuoka, N. (1999) *Struct. Fold. Des. 7*, 997−1008.
30. Xiang, B., Taylor, J. C., and Markham, G. D. (1996) *J. Biol. Chem. 271*, 1435−1440.
31. Zhang, R., G., E., Rotella, F., Westbrook, E., Huberman, E., Joachimiak, A., and Collart, F. R. (1999) *Curr. Med. Chem. 6*, 537−543.
32. Futer, O., Sintchak, M. D., Caron, P. R., Nimmesgern, E., DeCenzo, M. T., Livingston, D. J., and Raybuck, S. A. (2002) *Biochim. Biophys. Acta 594*, 27−39.
33. Kraulis, P. J. (1991) *J. Appl. Crystallogr. 24*, 946−950.
34. Laskowski, R. A., MacArthurs, M. W., Moss, D. S., and Thornton, J. M. (1993) *J. Appl. Crystallogr. 26*, 283−291.

BI0203785